Journal of Materials Chemistry B

ROYAL SOCIETY OF CHEMISTRY

PAPER

View Article Online
View Journal | View Issue

Cite this: J. Mater. Chem. B, 2026, 14, 2204

Radiopaque coating for improved implantability and *in vivo* imaging of neural probes

Axel Parys, [a] Federico Pazzaglia, [b] Wouter Van Lysebettens, [bc] Kristyna Kolouchova, [a] Lana Van Damme, [a] Jung Won Seo, [d] Andre G. Skirtach, [d] Jeroen Missinne, [b] Robrecht Raedt [c] and Sandra Van Vlierberghe *[a]

The invasive nature of brain implants remains a major limitation in neuromodulation strategies, often leading to chronic inflammation. To address this, soft coatings are applied on rigid probes to reduce the mechanical mismatch at the interface, or flexible probes are implemented accompanied by temporary stiffeners. This study presents a hybrid strategy integrating both approaches by applying a permanent hydrogel coating onto flexible neural probes. Moreover, we utilise the applied coatings as tool for post-operative non-invasive imaging *via* functionalisation of the hydrogel with 5-acrylamido-2,4,6-triiodoisophthalic acid (AATIPA), a monomer that increases radiodensity. Rheological measurements confirmed that AATIPA incorporation did not significantly alter the hydrogels' mechanical properties (storage moduli ranging from 139 ± 33.5 to 186 ± 55.5 kPa). Subsequently, we show that coated flexible probes exhibited a two-fold increase in critical buckling force compared to uncoated counterparts, indicating improved mechanical robustness evidenced through enhanced insertion performance in agarose brain phantoms. The mechanical contrast supports the dual purpose of the material in our application: the coatings provide stiffness to facilitate probe insertion in the dry state, while transitioning to a compliant, soft interface upon swelling, post-implantation. Finally, the radiodense coating enabled successful visualization of the probes in the hippocampus of a mouse model using μ-CT imaging. This approach offers a promising route for improving the mechanical and imaging performance of neural implants, potentially reducing reliance on post-mortem histology and enhancing real-time feedback in neuromodulation research.

Received 1st September 2025,
Accepted 20th January 2026

DOI: 10.1039/d5tb01967b

rsc.li/materials-b

1 Introduction

Epilepsy, Alzheimer's disease and Parkinson's disease are among the plethora of neural diseases that impact the quality of life for millions of people.[1] Over the last decade, various neuromodulation strategies have employed neural implants to alleviate patients' chronic symptoms.[2] For example, Deep Brain Stimulation (DBS)- a technique based on electrical stimulation – has demonstrated successful seizure control.[3] However, challenges related to efficacy, tolerability, and the invasive nature of metal implants remain unmet. In preclinical research, alternative approaches using optical stimulation try to overcome the issues associated with electrical stimulation.[4,5] For optogenetics, the commercially available implants are generally made of rigid materials such as silicon,[6] which exhibits a Young's modulus of 150–170 GPa.[7] While these materials excel in optical performance, their rigidity inhibits their long-term success when brought into contact with soft tissues (exhibiting Young's moduli in the low kPa range).[8] In an *in vivo* context, the naturally occurring micromotions caused by heartbeat and pulsatile movement of blood vessels result in an increasing amount of strain at the mechanically mismatched probe-tissue interface.[9] This strain serves as a major contributor to the chronic foreign body response, due to the constant aggravation of the local tissue. This process in turn stimulates glial scar formation, encapsulating the implant and impeding its performance. To overcome this challenge, research has drafted three critical parameters with regard to material choice for neural applications: biocompatibility, biostability, and biomimicry.[10] Failure to meet these

[a] Polymer Chemistry and Biomaterials Group, Department of Organic and Macromolecular Chemistry, Centre of Macromolecular Chemistry, Ghent University, Krijgslaan 291, Building S4, 9000 Ghent, Belgium. E-mail: Sandra.VanVlierberghe@UGent.be
[b] Centre for Microsystems Technology (CMST), imec and Ghent University, Technologiepark 126, 9052 Ghent, Belgium
[c] 4Brain, Department of Head and Skin, Ghent University, Corneel Heymanslaan 10, 9000, Ghent, Belgium
[d] Nano-Biotechnology Laboratory, Department of Biotechnology, Ghent University, Proeftuinstraat 86, 9000 Ghent, Belgium

principles will inevitably impact the long-term reliability and performance of the implants.

One method to address this issue entails the application of a soft coating around the rigid probe. Suitable candidate materials for this application are hydrogels, which have proven their importance in tissue engineering.[11] Two major classes of hydrogels can be distinguished based on the nature of the polymeric backbone: natural and synthetic. Natural material backbones such as collagen[12] and alginate[13] have demonstrated increased body acceptance towards neural devices. However, the synthetic alternatives, such as polyethylene glycol (PEG)[14] and polyvinyl alcohol (PVA),[15] have been found to be more tuneable in terms of molar mass, polymer architecture and hence, mechanical properties. Furthermore, specific surface chemistries have shown to impact tissue response, *e.g.* zwitterionic polymeric coatings have shown to significantly reduce inflammation responses.[16,17] Application dependant factors should also be considered, such as thermo-responsiveness, magneto-responsiveness, or conductivity.[18] The latter is often required in bioelectronic applications, where the most common strategies feature poly(3,4-ethylenedioxythiophene):polystyrene sulfonate (PEDOT:PSS).[19,20]

While the application of a coating layer is able to reduce the foreign body response (FBR), a trade-off between the mechanical benefits and increased implant dimensions must be considered. Calculations by Spencer *et al.*,[14] concerning PEG-dimethacrylate coatings on silica probes, have shown that coating thickness needs to exceed 100 μm to ensure adequate absorption of the occurring micromotions. Taking into account that the diameter of these probes are often smaller than 200 μm, the doubling in dimensions is found to be a significant disadvantage of the soft coating onto a rigid substrate. Although this coating can serve as a transition zone, the inherent stiffness mismatch between a rigid substrate and brain tissue cannot be overcome with this strategy.

Over the past decades, many researchers have shifted their efforts towards developing a new generation of neural devices that utilize soft and flexible materials to reduce the FBR.[21] The material flexibility allows the device to move with the micromotions, thereby alleviating the micromotion-induced strain at the probe-tissue interface. Most common materials employed for the fabrication of such flexible substrates are polymers, such as polyimide[22] and parylene C.[23] These materials have demonstrated excellent performance and biocompatibility, making them great candidates for neural probe materials.

Although promising, soft and flexible neural devices have challenges of their own. First, parylene C and polyimide exhibit a Young's modulus of 3 and 5 GPa, respectively, making the naming of these materials subtly misleading.[21] Although the 100-fold mechanical improvement over classical silicon probes is significant, the mismatch with the surrounding tissue remains several orders of magnitude. Furthermore, implantability is largely dependent on the bending stiffness – a parameter affected by design, dimensions, and material properties of the neural device.[24,25] As a result, a second challenge arises from the so-called "softness/implantability paradox".[7] The search for flexibility and miniaturisation, using softer materials, results in neural devices that are hard to handle and often not implantable on their own. Current innovations often focus on solving the latter issue. By utilising a removable aid or shuttle, one can achieve implantability of miniaturised flexible probes with cross-sectional dimensions below 100 micrometres.[26] The most common insertion aid involves the use of bioresorbable polymer coatings, providing a thick stiffening layer around the flexible substrates. Candidate materials in this regard include gelatin,[27] silk fibroin,[23] PEG[28] and maltose.[29] These bioresorbable polymers are per design non-permanent aids, thus neglecting the issue of their substrates' Young's modulus being several orders of magnitude higher than the surrounding tissue. As a result, the biomimicry requirement is not fully met and longevity issues are often inevitable.

Another issue relates to ethical considerations associated with animal testing, as we should continuously strive towards reducing the test subjects according to the 3R-principle.[30] Current research mainly encompasses post-experiment histology to verify the correctness of the surgical intervention in rat or mouse models.[31] This means that implantation failures such as bending often remain unnoticed, resulting in the need of additional animals to account for such failures. Efforts towards proper non-invasive imaging have been limited, with some papers exploring combinations of CT and MRI to monitor implant location.[31,32] However, non-adapted materials, whose radiopacity is hardly distinguishable from the surrounding tissue, result in tedious work-flows instead of rapid validation. Recently, we have reported the incorporation of a radiopaque monomer, the 5-acrylamido-2,4,6-triiodoisophthalic acid (AATIPA), into hydrogel materials to enable non-destructive μCT-analysis.[33,34] The 2,4,6-triiodinated isophthalic acid motif is a structural feature commonly found in FDA-approved iodinated contrast agents due to its excellent radiopacity and bioinertness. In AATIPA, this clinically validated motif has been functionalized with an acrylamide group to allow efficient and covalent incorporation into polymer networks *via* radical chain and/or step-growth polymerization.

Herein, AATIPA is incorporated into a PEG-based hydrogel coating which serves a dual role. First, we aim to exploit this coating as a stiffener enabling the implantation of flexible neural waveguides. However, in contrast with the shuttle or resorbable coating approach, herein, the coating also provides an imaging modality. To this end, our second target is to non-invasively monitor the implanted coated neural probes in the hippocampus of a mouse model using post-operative μCT. In terms of materials, acrylate-end-capped urethane-based PEG precursors (AUPs) are selected, which combine the mechanical properties of polyurethanes with the biocompatible properties of PEG. Their superior stiffness compared to conventional PEG-acrylates is hypothesized to be beneficial for the coatings' functionality as an implantation aid. Additionally, the end-caps feature three acrylate functionalities at each chain end to enable the formation of a densely cross-linked network exhibiting limited swelling. Limiting swelling is crucial as

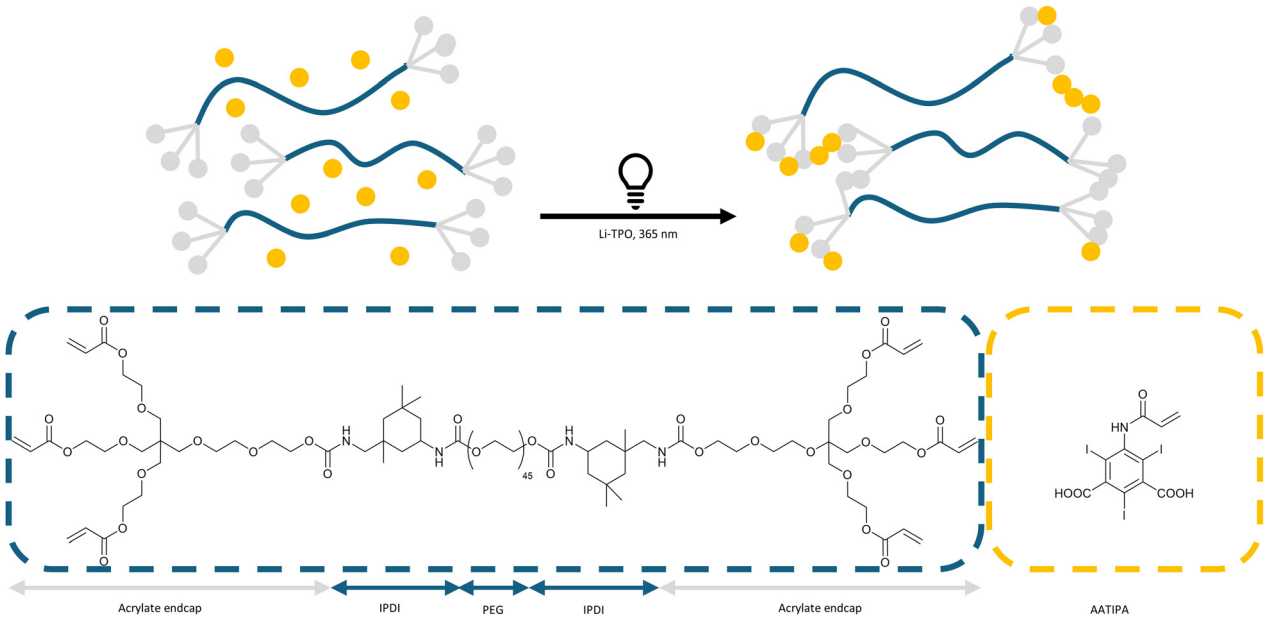

Fig. 1 Depiction of cross-linking of the hydrogel formulations under UV-irradiation. The mechanism is based on radical chain growth polymerization, connecting the acrylate and acrylamide functionalities in the mixture. Additionally, the molecular structures of the components constituting the hydrogel precursors are depicted. The used polymer, namely AUP, consists of a PEG backbone (M_w 2000 g mol^{-1}) that is coupled using urethane chemistry to tri-acrylate endcaps.

in vivo swelling will lead to intracranial hypertension which can severely impact neural function.

Herein, we also show the integration of AATIPA into cross-linked AUP networks and study its effect on the material properties (Fig. 1). Moreover, we investigate the impact of the covalent integration of the monomer on the biocompatibility of the resulting hydrogel material. We show that, following dip-coating and crosslinking, flexible neural probes exhibit a higher bending strength and improved implantability in an *in vitro* agarose model. Finally, we illustrate the control of radiopacity and possibility towards CT-imaging of the coated probes by gradually moving from *in vitro* towards *in vivo* imaging in a mouse model.

2 Materials and methods

2.1 Materials

The chemicals used in this research, were used as received unless otherwise stated. 3-(4,5-Dimethylthiazol-2-yl)-5-(3-carboxymethoxyphenyl)-2-(4-sulfophenyl)-2*H*-tetrazolium (MTS, Abcam, ab197010, 138169-43-4, Cambridge) ethyl(2,4,6-trimethylbenzoyl)-phenylphosphinate (TPO, Lambson Ltd HQ (West Yorkshire, UK), 84434-11-7), butan-2-one (Sigma-Aldrich (Diegem, Belgium), 78-93-3), lithium bromide (Sigma-Aldrich (Diegem, Belgium), 7550-35-8), dimethyl terephtalate (DMT, Sigma-Aldrich (Diegem, Belgium), 120-61-6), poly(ethylene glycol) 2000 g mol^{-1} (PEG-2K, Sigma-Aldrich (Diegem, Belgium), 25322-68-3), isophorone diisocyanate (IPDI, Sigma-Aldrich (Diegem, Belgium), 4098-71-9), phenothiazine (PTZ, Sigma-Aldrich (Diegem, Belgium), 92-84-2), sodium hydroxide (97%) (NaOH, Sigma-Aldrich (Diegem, Belgium), 1310-73-2), 5-amino-2,4,6-triiodoisophthalic acid (95%) (Sigma-Aldrich (Diegem, Belgium), 35453-19-1), acetonitrile anhydrous (99.9% + %) (CAN, Sigma-Aldrich (Diegem, Belgium), 75-05-8), 4-*tert*-butylcatechol (TBC, Sigma-Aldrich (Diegem, Belgium), 98-29-3), sulfuric acid (98%) (Sigma-Aldrich (Diegem, Belgium), 12777-87-6), acrylic anhydride (>90%, 500 ppm MEHQ as a stabilizer) (Fluorochem (Derbyshire, UK), 2051-76-5), ethoxylated and propoxylated pentaerythritol triacrylate (EPPETA, allnex (Wetteren, Belgium), 30374-35-7), deuterated chloroform (stabilized with silver foils +0.03% TMS, 99.8%) ($CDCL_3$, Euriso-Top (Saint-Aubin, France), 865-49-6), diethyl ether (stabilized with 5–7 ppm BHT, >99%) (Chem-lab NV (Zedelgem, Belgium), 60-29-7), butylated hydroxytoluene, (BHT, Innochem GmbH (Zurich, Switzerland), 128-37-0), Valikat bismuth neodecanoate catalyst (Umicore (Brugge, Belgium), 34364-26-6), Fluorobrite™ DMEM (Fluorobrite™, ThermoFisher, A1896701, N/A, Pittsburgh), calcein acetoxymethyl ester (Ca-AM, Merck, 56496, 148504-34-1, Darmstadt), propidium iodide (PI, ThermoFisher, 15438249, 25535-16-4, Pittsburgh), triphenylphosphite (TPP, Honeywell Fluka, 603-35-0). Ultrapure water, prepared using an Arium 611 (Sartorius, Goettingen, Germany) with the Sartopore 2 150 (0.45 + 0.2 μm pore size) cartridge filter, was used throughout the experiments.

The following products, obtained by synthetic efforts, were stored under inert argon and in absence of light: Li-TPO, AUPs, and AATIPA (Section 2.2.2). Experiments containing one of these products were performed under protection from direct light.

2.2 Methods

2.2.1 Fabrication of flexible probes. Dummy probes (non-functional, but fabricated out of same materials) for mechanical testing were fabricated on a 2-inch borosilicate substrate used as (temporary) carrier. The substrate was cleaned using an

alkaline detergent solution (RBS T 105) followed by rinsing using isopropyl alcohol and ultrapure water). Subsequently, a release layer (Acetyl-Cellulose 6 w/w% in acetone) was spin-coated (1000 rpm for 30 s). Prior to spin coating the probe materials, the substrate was plasma-treated (Diener Pico, 0.8 mbar, gas: air 95%, 0.8 mbar, 24 s, 190 W, 40 kHz generator). A layer of OrmoComp (Microresist Technology) was then spincoated and UV-cured for 35 seconds at 35 mW cm^{-2} in an inert atmosphere (N_2). The second OrmoComp layer was then applied similarly to the bottom layer (plasma treatment, spincoating, and UV-curing). Finally, the samples were hard-baked at 90 °C for 90 minutes. Then, probes with desired dimensions (115 × 120 × 15 000 (width × thickness × length) μm^3) were laser cut using laser ablation (picosecond YAG laser, wavelength 532 nm, 50 kHz, 1 W, 30 mm s^{-1}, 10 passes, 20 μm diameter laser spot size). Finally, the substrate was put in DI water (150 s at 75 °C) to release the probes from the glass carrier by dissolving the release layer.

2.2.2 Synthesis of hydrogel precursors. The syntheses of the acrylate-endcapped urethane-based polymer precursor (AUP) and 5-acrylamide-2,4,6-triiodoisophtalic acid (AATIPA) were performed according to previous work.[33,35] Moreover, lithium phenyl (2,4,6-trimethylbenzoyl)phosphinate (Li-TPO) was synthesized according to a previously described procedure.[36] Detailed information about the synthetic procedures are described in the SI S3.1.1. The success of the syntheses was verified with ^{1}H-NMR experiments on a Bruker Avance 400 MHz NMR Spectrometer at 21 °C. The data were analysed using Topspin 4.4.1 software provided by Bruker (Fig. S3–S5, SI).

2.2.3 Preparation of crosslinked films. Stock solutions were prepared by dissolving different amounts of AATIPA in 1 M NaOH solution (3.125 mL for each g AATIPA), and diluting the solution with ultrapure water to a total volume of 2 mL (per 1 g of polymer in the final mixture). These solutions were then used to dissolve the AUP polymer after which we added the photo-initiator Li-TPO (4 mol% with respect to the acrylates using a 40 mg mL^{-1} polymer solution in ultrapure water). The constituents of all formulations are summarised in Table 1. The mixture was briefly placed in a desiccator to remove air bubbles before injecting the solution between two parallel glass plates, separated by a 1 mm thick silicone spacer and covered with a thin poly(tetrafluoroethylene) sheet. Subsequently, the mould was irradiated from both sides with UV light (320–380 nm, 10 mW cm^{-2}) for 0.5 hour. The resulting films were washed with an ethanol/water mixture (70 : 30 v/v) for 24 h and with ultrapure water for another 24 h.

2.2.4 Characterization of crosslinked films

2.2.4.1 Determination of gel fraction (GF) and swelling percentage (S_w%). Polymerised hydrogel films were used to create samples with a thickness of 0.350 mm and a diameter of 7 mm, which were then freeze-dried. After the initial weighing ($W_{dry,1}$), the discs were incubated in ultrapure water for 24 h at 37 °C. The samples were subsequently washed and weighed again ($W_{swollen}$). Following this, the discs underwent a second freeze-drying cycle, and final mass measurements were taken ($W_{dry,2}$). The acquired data were used to determine the gel fraction and swelling percentage (S_w%) values, using the following equations:

$$\mathrm{GF}\ (\%) = \frac{W_{dry,2}}{W_{dry,1}} \times 100\% \quad (1)$$

$$S_w\% = \frac{W_{swollen} - W_{dry,2}}{W_{dry,2}} \times 100\% \quad (2)$$

detailed overview of obtained data can be found in SI Table S1.

2.2.4.2 High resolution magic angle spinning (HR-MAS) ^{1}H-NMR spectroscopy. We recorded the HR-MAS ^{1}H-NMR experiments on a Bruker AscendTM 500 MHz Avance III spectrometer equipped with a 4 mm ^{1}H/^{13}C Dual Channel HR-MAS probe, equipped with Z-gradients. The spinning frequency was set to 6000 Hz and the experiments were performed at 21 °C. (Fig. S6–S9, SI).

2.2.4.3 (Photo-)Rheology: frequency sweep and crosslinking kinetics. From hydrogel films, prepared as described in Section 2.2.3, samples with a 1.4 cm diameter were punched out. These samples were evaluated *via* oscillation rheology, performed on a Anton Paar Physica-301 rheometer. Herein, a frequency sweep from 0.1 to 10 Hz was applied (normal force F_N = 1.0 N, strain 0.1% and constant temperature of 25 °C).

To study the crosslinking kinetics, the same solutions as described in Section 2.2.3 were prepared. Of these solutions, 300 μL was placed between the spindle and bottom glass plate separated by a 0.35 mm gap, of an Anton Paar Physica-301 rheometer. Subsequently, the storage (G') and loss moduli (G'') were monitored over the course of 1 min without irradiation and 15 min during irradiation (365 nm: EXFO Novacure 2000 UV light source; 10 mW cm^{-2}). All obtained rheology spectra are depicted in SI Fig. S10–S17.

2.2.5 Dip-coating of flexible probes. Hydrogel precursor solutions were prepared using the method described in Section 2.2.2. Instead of creating hydrogel discs, the formulations were utilized as a dip-coating solution.

To ensure consistency, the probes were clamped in a holder mounted on a motorized stage (Kinesis motor: K-Cube® Brushed DC Servo Motor Controller) at a height of 1 cm from the tip. The tip of the probe was aligned with the surface of the

Table 1 Overview of amounts of network constituents in formulations used

Formulation	#AUP (g)	nAUP (mmol)	#LAP (mg)	nLAP (mmol)	#AATIPA (mg)	nAATIPA (mmol)	Volume H_2O (mL)
AUP0	1.000	0.285	17.21	0.059	0.000	0.000	3.24
AUP40	1.000	0.285	17.21	0.059	40.00	0.065	3.24
AUP80	1.000	0.285	17.21	0.059	80.00	0.130	3.24
AUP80C	1.000	0.285	17.21	0.059	160.000	0.261	3.24

hydrogel solution, and a controlled sequence was employed to displace the probe, effectively performing the dip-coating procedure. The sequence involved immersion of the probe for a length of 5 mm at a speed of 0.5 mm s^{-1}, a resting phase of 5 seconds, and a withdrawal step at 0.1 mm s^{-1}. After coating one layer, the probes underwent 30 s of irradiation to cross-link (405 nm, 10 mW) and form the hydrogel coating. These steps were repeated 5 times. Subsequently, the probes were vacuum-dried in a desiccator for 24 h to ensure dehydration and were finally stored under argon. In SI a picture of the setup S2 and pictures of dip-coated probes S18 can be found.

2.2.6 Mechanical characterization of coated flexible probes

2.2.6.1 Buckling force measurements. To perform the buckling force measurements, the probes (coated or uncoated) were clamped at a distance of 5 mm, measured from the tip, on a displacement-controlled holder using a Kinesis® motor (K-Cube® Brushed DC Servo Motor Controller). The holder was manually lowered until a 0.1 mm gap between the tip of the probe and a force gauge meter (MESUR Lite, Mark-10 M3-012) was achieved. Using Kinesis software connected to the motor, a fixed displacement sequence was applied to the holder and probe (a schematic figure of the setup is depicted in SI Fig. S1). The sequence consisted of a downward motion of 1 mm at a velocity of 0.1 mm s^{-1}, followed by a retraction motion of 1 mm at a velocity of 0.5 mm s^{-1}. During the displacement, the downward force was measured by the force gauge meter and recorded by its complementary software, MESUR Lite. The data were exported as an Excel file for further processing. Processing included the determination of the critical buckling force, defined as the inflection point in the force-displacement curve. This point was approximated by the maximum compressive force prior to structural instability. From the critical buckling force, an estimation of the Young's modulus was deduced, using the following equation:

$$F_{\text{Euler}} = \frac{\pi^2 EI}{(kL)^2}, \quad \text{where } I = \frac{W \times T^3}{12} \tag{3}$$

with F_{Euler} equalling the Euler's buckling force (N), I as the second moment of area (m^4), E the Young's modulus (Pa), L the probe length (m), W the width of the probe (m), T the thickness of the probe (m) and k a length correction factor. Depending on the boundary conditions of the probe-tissue contact, the value of k can vary. Herein, since the probe is clamped at the top, the value k equals 0.7.[23]

2.2.6.2 Agarose insertions. Prior to the experiments, agarose gels (0.6 w/v%) were prepared by dissolving agarose powder in ultrapure water at 95 °C under continuous stirring. Subsequently, the solution was cooled to 35 °C and poured into cuvettes. The cuvettes containing the agarose mixture were placed in the refrigerator to allow solidification.

Agarose insertions were performed as follows: the probes were mounted onto a force gauge meter using a custom-made holder, ensuring precise alignment. The exposed length of each probe was adjusted to 5 mm, and the tip of the probe was positioned 1 mm above the surface of the agarose gel. The force gauge meter with the probe was displaced using a motorized stage to perform the insertion sequence. This sequence consisted of a controlled insertion and retraction of 5 mm at a velocity of 0.1 mm s^{-1}. During the displacement, the force was measured by the force gauge meter and recorded by its complementary software, MESUR Lite. The data were exported as Excel files for further processing. Additionally, the experiments were visually recorded using cameras positioned at the front and side of the gel.

2.2.7 Stability testing. To evaluate the structural and mechanical stability, coated and uncoated probes were subjected to incubation experiments in phosphate-buffered saline (PBS, pH 7) at 37 °C. The probes were evaluated visually weekly, using optical microscopy (reichert-jung polyvar MET, 5× objective with a 0.8× multiplier, medium aperture, 2× gain). The coating thickness was measured at predefined positions along the shaft of the probe (0.5, 1 and 1.5 mm from the tip) to ensure consistent comparison and analysis.

2.2.8 Atomic force microscopy (AFM)

2.2.8.1 Cantilever preparation. The cantilever used throughout the experiment was the All In One Tipless-D model (Budget-Sensors). A glass bead with a radius of 6 μm (Polysciences, Inc.) was affixed to the free end of the cantilever using UHU Epoxy Extra Strong adhesive. Throughout imaging, the following cantilevers were used: DNP-S-B (Bruker) and ATEC CONT (Nanosensors).

2.2.8.2 Sample measurements. All atomic force microscopy (AFM) measurements were performed on 35 mm plastic Petri dishes. The AFM system used throughout the experiments was the NanoWizard 4™ (JPK Instruments/Bruker), equipped with a manual stage. Prior to each measurement, the cantilever sensitivity was determined and calibrated to obtain accurate values for the spring constant and resonance frequency.

At the start of each measurement, transmission images were acquired. Mechanical properties were assessed at four distinct points on both coated and uncoated regions of the samples. Measurement parameters included a 3 × 3 pixel grid, a scan size of 10 μm, a default setpoint, and a Z-speed of 2 μm s^{-1}, with all measurements conducted in Z-stepper mode. Next, force mapping was carried out and the data were recorded.

Initially, the Young's modulus of the dry samples was measured. Subsequently, the probes were immersed in phosphate-buffered saline (PBS) for 48 hours, after which the Young's moduli measurements were repeated.

For imaging experiments, Advanced QI imaging modes were used. Parameters for each measurement included 100 × 100 pixels, a scan size of 1 μm × 1 μm (ATEC CONT) and 2 μm × 2 μm (DNP-S-B), a default setpoint, and a Z speed of 2 μm s^{-1}, with measurements conducted in Z stepper mode. Next, force mapping was conducted and data were saved. Probes were submerged in PBS throughout the imaging procedure.

2.2.8.3 Data processing. Force map data obtained during AFM measurements were analysed using the JPK Data Processing software. Each force map contained mechanical

information from nine distinct points, including parameters such as height and stiffness. Individual force curves were extracted from the maps and processed through a series of steps to ensure accurate and reliable analysis.

First, the voltage deflection (V-deflection) of each force curve was calibrated following each measurement. To reduce noise and improve data quality, smoothing was applied using the Gaussian model, selected as the default smoothing method.

Subsequently, baseline subtraction was performed by calculating the average value of the force curve and subtracting it from the entire dataset, thereby normalizing the curve. The contact point—essential for determining mechanical properties—was identified by locating the intersection of the force curve with the zero-force line.

Finally, elasticity fitting was conducted to calculate the Young's modulus from the processed force curves. The built-in Hertz model was employed for this calculation. To obtain the images, heights of the pixels were calculated based on the individual force curves.

2.2.9 *In vitro* biocompatibility: MTS and live/dead assays. Human foreskin fibroblasts (HFF) were cultured in basic culture medium (DMEM, 10% FBS, 1% penicillin/streptomycin). A 96-well plate was seeded with 10 000 cells per well.

For the direct contact test, 6 mm diameter discs were sterilized by submerging them in 70% ethanol (EtOH) for 24 h, with EtOH being refreshed after 12 h. The discs were then washed with sterile PBS and subjected to UV-C irradiation for 30 min. 24 hours following cell seeding in the 96-well plate, the discs were placed on top of the cells. Biocompatibility testing was conducted at 1, 3 and 7 days following the placement of the samples on the cells, with media replacement every 2–3 days.

Due to their size, the probes were assessed *via* indirect leaching tests. The probes were incubated in basic culture medium for 1, 3 and 7 days. After incubation, the leached media were applied to the cells for 24 h.

Cytocompatibility was evaluated using both a live/dead viability assay (with calcein-acetoxymethyl ester (Ca-AM) and propidium iodide (PI)) and an MTS assay to assess the metabolic activity. For the live/dead assay, 2 μL of a 1 mg mL^{-1} stock solution of both Ca-AM and PI was added to each 1 mL of PBS. 0.15 mL of the resulting solution was added to each well and incubated in the dark for 10 min at room temperature. Living cells were visualized using a fluorescence microscope with a GFP filter for Ca-AM, and dead cells were visualized with a Texas Red (TxRed) filter for PI. The live/dead ratio was quantified using ImageJ software, which enabled the counting of both living and dead cells.

For the MTS assay, the culture medium was replaced with 100 μL of fresh medium, and 20 μL of MTS solution was added to each well. The plates were incubated in the dark (covered with aluminum foil) on a shaker at 37 °C for 1.5 h. After incubation, 100 μL of supernatant was transferred to a new 96-well plate, and absorbance was measured at 580 nm using a spectrophotometer.

2.2.10 Micro-computed tomography. μCT images were acquired with a preclinical X-CUBE micro-CT system (MOLECUBES; Ghent, Belgium), in "High-resolution mode" as previously described.[37] This mode encompassed a continuous scan, tube voltage of 50 kV, tube current of 350 μA, 960 projections (each projection has 1 averaging), acquisition per projection 125 ms, total acquisition time 150 s, dose per one bed position 166 mGy. The X-ray source (X-ray tube) was a fixed tungsten anode with a 0.8 mm aluminium filter and a non-variable focal spot size of 33 μm. The flat-panel detector was based on CMOS technology (14-bits) using a CsI scintillator. It consists of 1536 × 864 pixels for an active area of 115 mm × 65 mm with a pixel size of 75 μm. Further hardware and software details are described in previous work.[37]

μCT imaging was performed at the Core ARTH infinity facility at Ghent University (Belgium).

2.2.11 Animals. Implantations were performed in 6 adult male C57Bl/6 J mice (8 weeks old), obtained from Envigo (he Netherlands). Animals were housed under environmentally controlled conditions (temperature 21–22 °C, relative humidity 40–60%) at a fixed 12-h light/dark cycle. Food and water were available *ad libitum*. Prior to the start of surgery, all animals were group housed. Animals were housed individually after implantations. All procedures were conducted in accordance to the European Directive 2010/63/EU and were approved by the Animal Experimental Ethical Committee of Ghent University (ECD 24–57).

2.2.12 Stereotaxic implantations. Mice were anesthetized with isoflurane (5% at 2 L min^{-1} for induction, 2% at 0.5 L min^{-1} for maintenance) and head mounted into a stereotaxic frame (Neurostar Robot Stereotaxic system, Neurostar, Tubingen, Germany). Body temperature was monitored and kept stable at 37 °C using a rectal probe and a feedback controlled heating pad. A midline incision was made in the scalp to expose the skull. Two holes were drilled above the hippocampi followed by implantation of a AUP0-coated probe in the right hippocampus and a glass probe in the left hippocampus (stereotactic coordinates: −2 mm AP and −/+1.5 mm ML relative to bregma, −2 mm DV relative to dura, implantation speed = 0.05 mm s^{-1}). In three animals the glass probes were exchanged by AUP160 coated probes. Extracranial segments of the probes were fixated to the skull using clear C&B-Metabond (Parkell, USA). Afterwards, the skin was closed with non-degradable stitches and animals were observed after waking up from anesthesia, followed by transfer to home cage.

2.2.13 *In vivo* CT-imaging. At 3 days and 6 weeks post-surgery, mice were anesthetized as described previously and μCT imaging was performed using a Molecubes X-CUBE system (Bruker, Belgium) with the following parameters: 50 kV X-ray voltage, 350 μA current, 960 exposures at 32 ms each, and binning factor of 1. Images were reconstructed using an iterative algorithm (ISRA) at 50 μm isotropic voxel size. After conclusion of the μCT imaging, animals were euthanized with an overdose of sodium pentobarbital (1500 mg kg^{-1}, i.p.).

μCT imaging was performed at the Core ARTH infinity facility at Ghent University (Belgium).

2.2.14 Histology. After conclusion of the μCT imaging, animals were euthanized with an overdose of sodium

pentobarbital (1500 mg kg^{-1}, i.p.) and transcardially perfused with phosphate-buffered saline (PBS) followed by paraformaldehyde (4%, pH 7.4). The brains were isolated and were post fixed in paraformaldehyde (4%, pH 7.4) for 24 h and subsequently cryoprotected in a sucrose solution of 10-20-30% at 4 °C, snap-frozen in isopentane and stored in liquid nitrogen at −196 °C. After 1 hour at −20 °C, coronal cryosections of 30 μm were made using a cryostat (Leica, Germany). Sections containing the implantation tract were selected and processed for anti-NeuN staining to visualize neurons.

The sections were rinsed twice for 5 min in distilled water (dH_2O) followed by incubation in 0.5% and 1% H_2O_2 for 30 and 60 min respectively to block endogenous peroxidase activity. After washing twice for 5 min in PBS, sections were incubated in blocking buffer made of PBS containing 0.4% Fish Skin Gelatin (FSG) and 0.2% Triton X for 45 min to block non-specific antibody binding sites. The sections were then incubated in primary antibodies to visualize neurons with Chicken Anti-NeuN (1 : 1000, ABN91, Sigma Aldrich) for neuron staining, rabbit anti-GFAP (1 : 1000, ab7260, Abcam) to visualize astrocytes and rabbit anti-Iba1 (1 : 1000, 019-19741, Wako) to visualize microglia, diluted in blocking buffer for 1 hour at room temperature and subsequently overnight at 4 °C. On the next day, the sections were washed twice in blocking buffer for 10 min followed by incubation in secondary antibody Alexa Fluor Goat anti chicken (594 nm) (1 : 1000, AB0078, Abcam) diluted in blocking buffer for 1 hour at room temperature in darkness and subsequently rinsed in PBS (2 × 5 min). Sections were mounted on glass slides and cover slipped using Vectashield H1000 mounting medium (Vector Laboratories, USA) to prevent photo bleaching. Slices were scanned with a fluorescent microscope (Panoramic 250, 3D Histech, 40× magnification).

2.2.15 Evaluation of neuronal damage neural detection. Slices showing implantation tract were selected, and every other slice with a total of 3 slices per animal were analysed in QuPath (v0.6.0). Implantation tracts were manually annotated and a reference line was drawn to define tract orientation. A standardized 1000 μm × 700 μm analysis region was computationally aligned to each tract using the reference line midpoint. Image preprocessing included rolling ball background subtraction, median filtering, followed by quantile-based adaptive thresholding. NeuN+ neurons were detected using QuPath's watershed algorithm.

The other markers were studied as follows: concentric ring regions were computationally generated at increasing distances from the implant tract boundary (50, 100, 150, 200, 250, 300, 350, 400, 450, and 500 μm). The implant tract itself was defined as distance 0 (lesion region).

Direct fluorescence intensity measurements were performed by systematic pixel sampling within each distance region. Every 10th pixel was sampled to ensure representative coverage while maintaining computational efficiency. At each sampled pixel, RGB values were extracted corresponding to GFAP (red channel), Iba1 (green channel), and DAPI (blue channel) fluorescence intensities. Background-subtracted values were used to quantify inflammation.

2.2.16 Elemental analysis. The C/H/N composition of freeze-dried hydrogels was measured using PE 2400 Series II CHNS/O analyser (PerkinElmer, USA) in combustion mode (pure oxygen). Mass of all samples was 1.5 ± 0.1 mg (all samples were weighted with a calibrated scale with certainty of 0.001 mg). The absolute uncertainty of CHN determination is ≤0.3 abs.%. The instrument was freshly calibrated before use. All samples were measured in 2 independent experiments. The results are depicted in SI Table S2. The iodine content in freeze-dried samples was determined *via* modified Leipert method, as previously described.[34]

2.2.17 Statistics. Triplicate measurements were standard, except for NMR (n = 1), gel fraction and swelling percentage (n = 6), AFM (n = 2 samples and up to 40 measurements over each measured area) and elemental analysis (n = 2). All acquired data were processed with the built-in functions of Microsoft Excel, if not mentioned otherwise in the relevant section. Statistical significance was considered at $p < 0.05$. All values are expressed as mean ± standard error of the mean. To visualise the data, GraphPad Prism version 8 was utilised. Statistical significance was considered at $p < 0.05$. All values are expressed as mean ± standard error of the mean. For all non *in vivo* data, *t*-tests were used to evaluate the statistical significance.

For statistical analysis of *in vivo* data, mean fluorescence intensity values were calculated for each distance category by averaging across all sampled sections within each region for each animal and implantation site. Distance categories were grouped as follows: 0–100 μm, 100–200 μm, 200–300 μm, 300–400 μm, and 400–500 μm. Linear mixed-effects models were fitted with GFAP, Iba1, and Neun+ fluorescence intensity (Arbitrary Units) as dependent variables, which were log-transformed prior to analysis to improve model convergence and meet normality assumptions. The models (log(intensity) ~ probe type × Distance + (1|Animal ID)) included probe type (glass control *vs.* hydrogel-coated flexible probe) and distance categories as fixed effects. Animal ID was included as a random intercept to account for repeated measurements within animals. Model selection was performed using Akaike Information Criterion (AIC), comparing main effects *versus* interaction models. Statistical significance was considered at $p < 0.05$. All values are expressed as mean ± standard error of the mean.

3 Results & discussion

3.1 Characterisation of impact of AATIPA on hydrogel network

The syntheses were carried out successfully as detailed in Section 2.2.1 and analysed using ^{1}H-NMR spectroscopy. Using the hydrogel precursors, four formulations (Table 2) were prepared to investigate the effect of AATIPA content on the material properties.

No significant differences ($p > 0.5$) were found between the gel fraction (GF) of AATIPA-containing samples (AUP40, AUP 80 and AUP160) and the AATIPA-free reference (AUP0). All

Table 2 Physico-chemical properties of AUP-based hydrogel formulations: amount of AATIPA monomer (wt%), amount of iodine in dry (I_{dry}) and in swollen ($I_{swollen}$) state in the formulations, gel fractions (GF), swelling percentages (S_w%), storage moduli (G'), loss moduli (G''), compressive storage moduli (E') and radiodensity (RD) values. The table reports the data as means ± standard deviations (SD)

Formulation	AATIPA (wt%)	I_{dry} (wt%)	$I_{swollen}$ (wt%)	GF (%)	S_w% (%)	G' (kPa)	G'' (kPa)	E' (MPa)	RD (HU)
AUP0	0.00	N/A	N/A	94.8 ± 2.3	405 ± 18.0	147 ± 22.8	1.34 ± 0.48	0.44 ± 0.07	−132 ± 117[a]
AUP40	3.79	2.32	0.52	94.6 ± 2.1	448 ± 32.6	195 ± 48.9	1.95 ± 0.83	0.58 ± 0.15	215 ± 134
AUP80	6.78	4.15	0.80	96.8 ± 1.3	519 ± 11.6	165 ± 27.1	1.41 ± 0.41	0.50 ± 0.11	332 ± 188
AUP160	11.7	7.17	1.20	95.6 ± 0.9	600 ± 22.7	155 ± 14.3	1.25 ± 0.16	0.47 ± 0.04	587 ± 176

[a] Negative HU is the result of air bubbles between the hydrogel pieces.[33]

hydrogels showed a GF above 90%, which shows the efficient incorporation of PEG and AATIPA of the precursor blends. These findings contrast previous studies, where the addition of AATIPA in gelatin and poly-ε-caprolactone (PCL) precursors resulted in a decrease in GF and conversion.[33,34] This suggests that the AUP precursor is more effective towards incorporating AATIPA into the hydrogel network compared to methacrylated gelatin and ene-functionalized poly-ε-caprolactone (PCL) systems.[33,34] To further confirm the successful incorporation of the precursors, HR-MAS NMR experiments were conducted. These analyses verified the absence of residual acrylamide or acrylate in the washed samples (SI S6–S9). With regard to the swelling ratio (S_w%), we observed an increasing S_w% from 405.3% (AUP0) to 600.0% for samples with the highest AATIPA content (AUP160). The increase in swelling ratio (S_w%) can be attributed to the presence of AATIPA's anionic carboxylate groups. These carboxylate salts are formed during the preparation of the hydrogel precursor. Hence, AATIPA is effectively integrated into the hydrogel network in its carboxylate salt form, thereby enhancing the hydrophilicity of the system at higher AATIPA concentrations. This trend was also observed in previous studies reporting on the incorporation of AATIPA in poly(ε-caprolactone) (PCL)-based networks.[33] Next to indicating that the hydrophilicity increase could be the lead cause, they suggest that the formation of AATIPA oligomers between cross-links results in an increased mesh size. They supported this hypothesis with rheological measurements, showing a clear decrease in storage modulus upon increasing the AATIPA content. In contrast, our frequency and *in situ* cross-linking kinetics rheological experiments did not reveal any statistical differences in storage moduli across the various formulations, with values ranging from 147 ± 22.8 kPa to 195 ± 48.9 kPa. This suggests that, unlike step-growth cross-linked PCL systems, the chain growth polymerisation mechanism of the AUP hydrogels enables a more homogeneous incorporation of AATIPA. As a result, variations in AATIPA content have a limited effect on the mechanical properties of the final material.

The storage moduli can be correlated to the compressive moduli E', using the following equation:[38]

$$E' = 2G'(1 + \mu) \quad (4)$$

with G' the storage modulus and μ the Poisson number (0.5 for ideal rubbers, which can be used as stiffness approximation method for hydrogels).[38–40] Utilising this formula, the Young's moduli of our hydrogels were determined to be around 0.5 MPa (see Table 2). These values correspond to what was previously reported in literature for AUP materials with similar molecular weight PEG backbone, not containing AATIPA.[35,39]

Next to frequency sweep experiments, we performed cross-linking experiments during photo-rheology (SI Section S3.6). In all cases, the gel point was reached within 2 seconds, showing that the addition of the AATIPA monomer does not influence the cross-linking kinetics.

3.2 Application and stability of coating on flexible neural probes

Next, the hydrogel precursors were exploited to coat flexible probes. The procedure consisted of five coating layers applied with a retraction speed of 0.05 mm s^{-1}. This resulted in a coating with a mean thickness of 61.2 ± 3.5 μm after coating and 59.4 ± 2.70 μm after drying. This ensured maximal uniformity over the whole length of the probe while obtaining a thickness above 50 μm. The 50 μm thickness has been carefully chosen as a target to ensure sufficient stiffening of the probes and to ensure sufficient volume for CT-visualisation.

Using the fabricated probes, we executed a stability test to study whether prolonged incubation in PBS at 37 °C would impact the coating. As depicted in Fig. 2C, the thickness measurements along the shaft of the probes did not result in statistically significant variations. This showed that over a period of 3 weeks, the hydrogel coating is not degrading significantly. The stability over the first three weeks is essential as the FBR is mainly caused by the mechanical mismatch during the initial period after implantation.[7] We did not observe other defects occurring during the incubation of the probes. Additionally, we performed an assessment after 18 weeks to evaluate the coating stability throughout a longer time span. No significant differences were found between the results obtained in week 18 compared to the previous measurement points. Previous studies have shown that ester-linked hydrogels, such as poly(ethylene glycol) diacrylate (PEGDA), undergo degradation *via* first-order kinetics driven by ester hydrolysis.[41,42] The hydrolysis rate is governed by the mesh size and swelling degree, allowing degradation half-lives to be tuned from weeks up to months. Consequently, this study utilized a highly cross-linked network constituting a low molecular weight PEG backbone, thereby enhancing overall stability of the coating. Previous studies have also shows that PEGDA's *in vivo* degradation mirrors the *in vitro* (1× PBS at 37 °C) studies.[42,43]

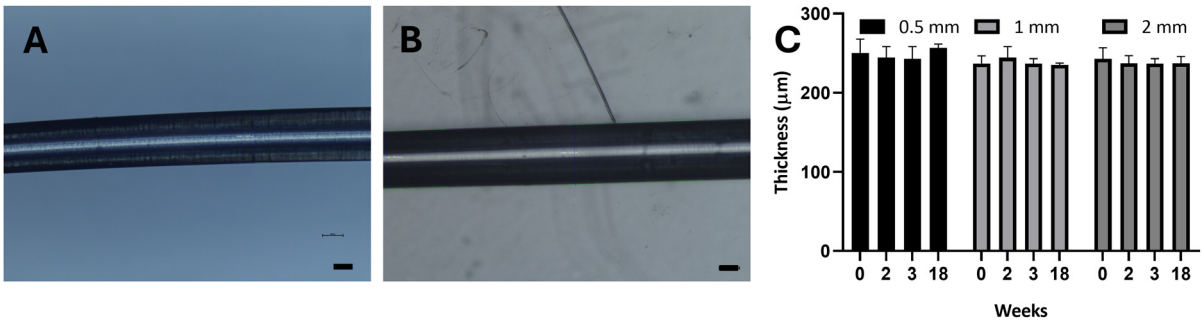

Fig. 2 (A) Depiction of coating thickness before and (B) after drying achieved *via* dip-coating. Scale bar 100 µm. (C) Thickness of coating after 0, 2, 3, and 18 weeks of incubation in PBS at 37 °C. The samples were measured at 3 fixed positions starting from the tip of the probe (0.5, 1 and 2 mm), n = 3 for each timepoint.

3.3 Improved mechanical performance of coated flexible probes

With an established coating protocol, we proceeded with studying the mechanical properties of the coated probes. First, we demonstrated the probes' behaviour under axial pressure by bending/buckling the probes against a rigid surface. From these measurements, we derived the maximum axial compressive force the probe can withstand before becoming unstable, which is generally named the critical load or buckling force. Uncoated probes with 115 × 120 × 15 000 (width × thickness × length) µm^3 dimensions demonstrated a buckling force of 15.2 ± 2.0 mN. Once coated, this critical load more than doubles to 33.0 ± 1.5 mN. During implantation, mechanical failure can occur when the insertion or shear forces sensed by the probe exceed the critical load, resulting in bending of the shaft.[7] This suggests that the coating is able to provide additional support during mechanical insertion and handling.

The critical load can be utilised to estimate the Young's modulus (E) of the probe by employing Euler's buckling theoretical framework.[23] Using eqn (5) (method Section 2.2.6.1), the Young's modulus of the uncoated probes was estimated to be 1.29 ± 0.15 GPa, which is in line with literature.[44] However, this theoretical formula is ill-suited to make estimates for multilayered systems such as hydrogel-coated probes. As a result, we relied on a complementary approach to estimate the Young's modulus of the coating material. Given the interface-focused nature of the application, we decided upon atomic force microscopy (AFM) measurements to assess the surface properties of the coatings. The Young's modulus of the coated samples in the dry state was determined to be 6.77 ± 4.31 MPa. Upon swelling, the coatings exhibited softening, with the modulus decreasing 10-fold to 0.76 ± 0.15 MPa. These findings align with previously reported values for related hydrogel systems, such as poly(ethylene glycol) diacrylate (PEGDA).[45,46] For instance, Yadavalli *et al.* reported Young's moduli of 4.33 ± 0.28 MPa and 2.85 ± 0.35 for dry and swollen PEGDA (Mw 575 g mol^{-1}), respectively.[47] In the present study, a PEG backbone with a slightly higher molecular weight was used, resulting in an increased swelling capacity of the hydrogel. Consequently, a more pronounced difference in Young's modulus between the dry and swollen states was observed. The mechanical contrast supports the dual purpose of the material in our application: the coatings provide stiffness to facilitate probe insertion in the dry state, while transitioning to a compliant, soft interface upon swelling, post-implantation. The Young's moduli in swollen state found in this work *via* AFM are also comparable to the results obtained in Section 3.1, where the rheological analysis was discussed. Slight deviations in the Young's moduli can be explained by the nature of the experimental techniques, but overall, the combined data result in an understanding of the coating layer's mechanical performance. While our results (0.5–0.8 MPa) have not reached the ideal range of the Young's modulus of brain tissue (0.1–100 kPa), literature shows that by lowering the Young's modulus beyond a few MPa's, no additional gain can be achieved in terms of lowering the inflammatory response of surrounding tissue.[48] Therefore, we deployed our synthetic degree of freedom to limit swelling and to improve the stiffening effect, instead of further optimising the Young's modulus. Atomic force microscopy (AFM) measurements also included force mapping to assess the microscale surface roughness of the samples. As shown in Fig. 3, the roughness of the uncoated substrate remained below a variance of 20 nanometres. In contrast, measurements on the coated regions revealed more pronounced height variations, attributed to the higher swelling capacity of the hydrogel coating. While the swelling process accentuates surface inhomogeneities, the overall height variations remains below 40 nanometres. We further studied the probes' performance in brain phantom implantations. To this end, we prepared an 0.6 w/w% agarose gel, which is commonly used as a brain tissue phantom due to its comparable mechanical properties (Young's modulus ≈ 10 kPa).[49] Mechanical success in this case is achieved when the buckling force F_{Euler} exceeds both the $F_{\text{Insertion}}$ and F_{Shear}. $F_{\text{insertion}}$ represents the peak load necessary to penetrate the agarose surface, which is about 1 mN.[50] As can be observed in Fig. 4A1 and B1, both the coated (AUP0) and uncoated probes are able to penetrate the agarose gel surface without mechanical failures. Starting from the initial penetration of the agarose gel surface, an increasing shear force (F_{shear}) is experienced during further insertion of the probe into the agarose gel. This shear force arises from the friction between the probe and its surroundings along the shaft of the probe.

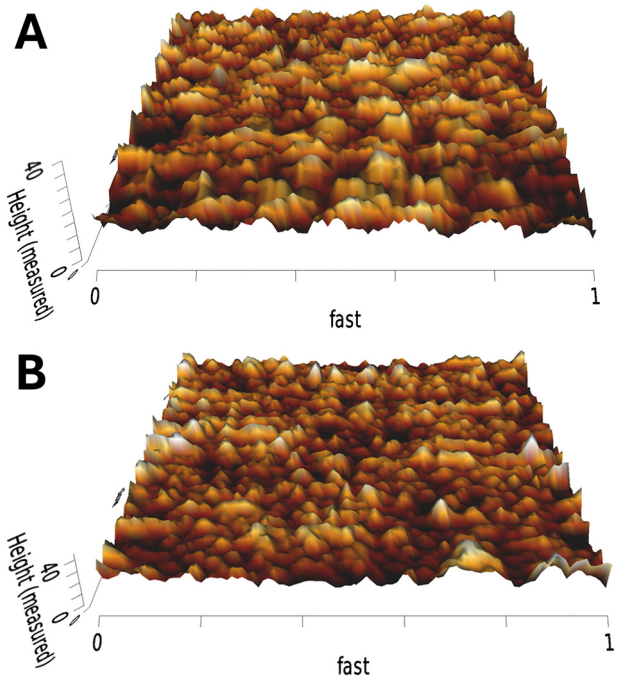

Fig. 3 AFM 3D-maps of 1 × 1 μm sections of uncoated (A) and coated (B) probes.

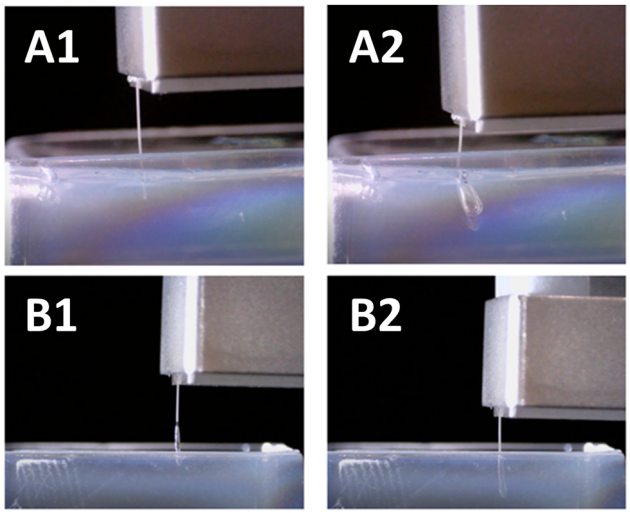

Fig. 4 Pictures taken during the agarose (0.6 w/w%) insertion experiments after the initial insertion through the agarose gel surface of 115 × 120 × 1500 μm^3 probes without (A1) and with (B1) coating (AUP0). A2 shows probe without coating during further insertion, and B2 the probe with coating. In A2, bubble formation was observed resulting from air being introduced in the cavity generated by bending of the probe.

Targeting an implantation depth of 4 mm, the probes undergo forces up to 30 mN during this phase. As discussed in Section 3.3, the critical force of the uncoated probes was only, 15.2 ± 2.0 mN. This resulted in significant bending of uncoated samples. In contrast, the coated probes with critical force of 33.0 ± 1.5 mN did not exhibit signs of mechanical failures during the agarose implantations. Finally, we inspected the probes after retraction to verify the absence of defects resulting from the process. In all cases, no signs of adhesiveness failure was observed, meaning that the adhesive strength between the probe and coating is able to resist at least 30 mN as this was the maximal force that was measured during the implantations.

3.4 *In vitro* biocompatibility assays

After confirming the mechanical properties of the hydrogel materials and the coated probes, the envisioned biomedical application requires a study towards the effect of the AATIPA monomer on the biocompatibility of the hydrogel coating. To this end, the hydrogels were brought in direct contact with cultivated human foreskin fibroblasts. We evaluated the cytocompatibility using a live/dead viability assay and the metabolic activity with an MTS assay. The results (Fig. 5) show a slight decrease of cytocompatibility at higher AATIPA content. However, all samples show biocompatibility well above the ISO standard (cell viability >70%, ISO 10993).

A similar analysis was performed on the neural probes, with and without hydrogel coating. During these tests, no significant difference was observed between the coated and uncoated probe samples. Overall, this implies that the probes, hydrogel and AATIPA content (at least up to 50 mg mL^{-1}) are viable candidates to serve biomedical applications in terms of cytocompatibility and metabolic activity.

3.5 AATIPA increases radiopacity in AUP hydrogels

Next, we proceeded by establishing the conditions required to visualise micrometre scale probes *in vivo*, using μCT. Therefore, we gradually went through a series of experiments, where we aimed to ensure a proper contrast between the probe and its surroundings at each step. First, we utilised hydrogels made from the formulations listed in Table 1 to study the radiopacity of the hydrogels upon increasing AATIPA content. As depicted in Fig. 6, even the lowest amounts of AATIPA resulted in a radiodensity (RD) of 215.3 ± 133.7 HU. The AATIPA content in the final dried materials was determined *via* elemental analysis, quantifying the iodine content (Table 2). To validate the elemental analysis results, the iodine content of swollen hydrogels was plotted against their measured radiodensity. This revealed a linear correlation (Fig. 6A), with an increase of approximately 590 HU per wt% iodine. This value is comparable with previous reports,[51] confirming that the radiodensity of the samples corresponds well with the iodine content determined analytically. As the brain tissue has an RD of approximately 30 HU, this should theoretically be distinguishable. However, we were targeting to implant micrometre sized probes with a 50 μm coating layer. In general, it has been established that a higher difference in radiopacity between the implant and the surrounding tissue leads to a decrease in smallest volume to enable reliable material detection.[34] The RD steadily increased with an increase of AATIPA loading into the hydrogel samples. Sample AUP160 reached a RD of 587.1 ± 175.7 HU. The tuneability of radiodensity is important when working with smaller constructs, as previous studies have shown that the spatial resolution of the μ-CT devices is dependent on the

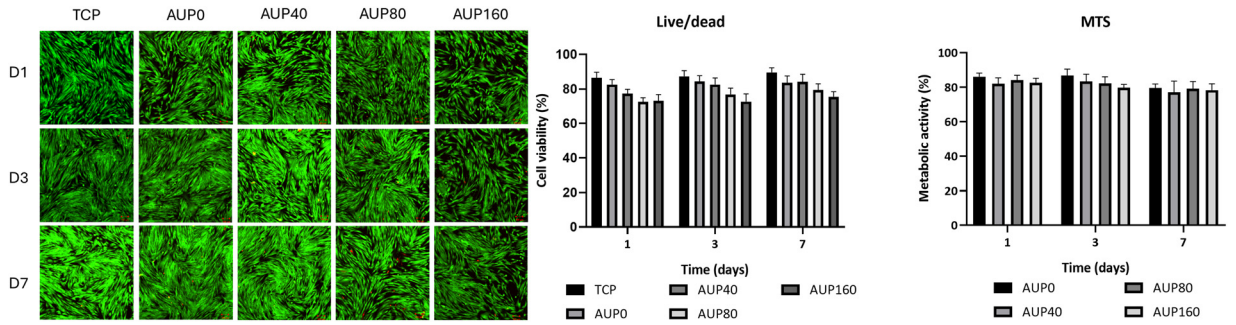

Fig. 5 Human foreskin fibroblasts cultivated in direct contact without (TCP) and with hydrogel discs containing increasing amounts of AATIPA. Live/dead staining and MTS assays were performed on days 1, 3 and 7 after cell seeding. Scale bar equals 200 μm. n= 3 for each treatment.

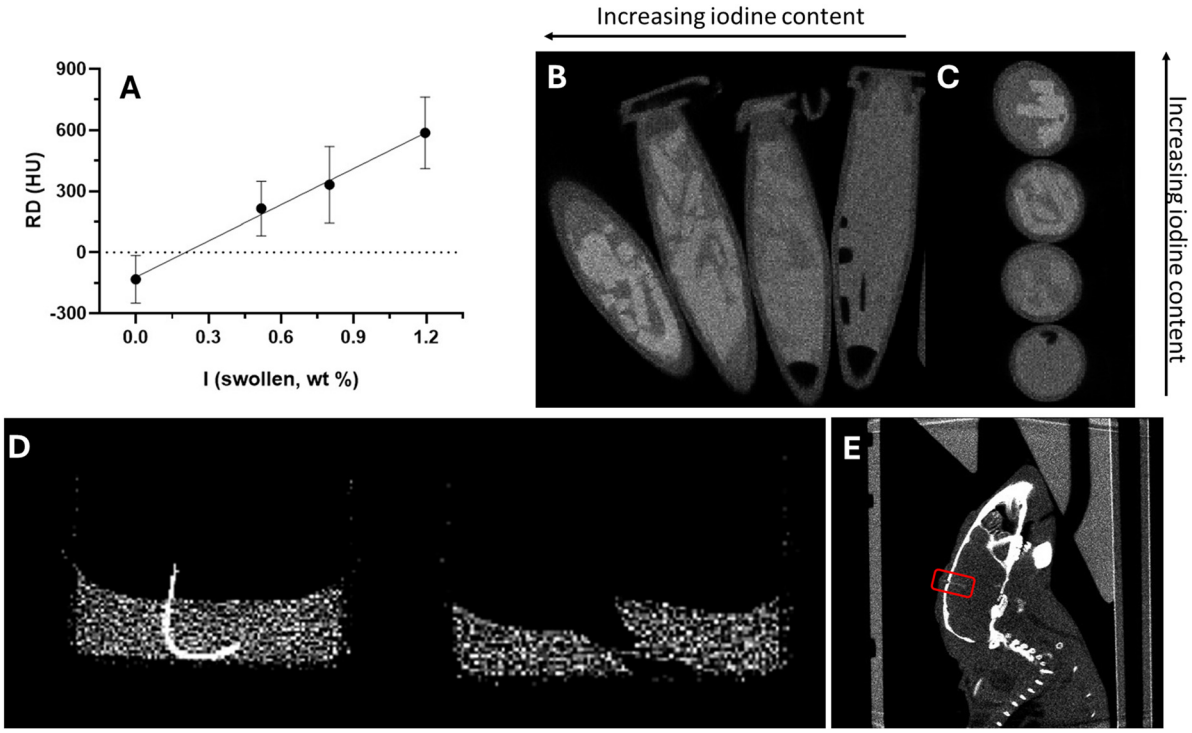

Fig. 6 (A) Radiopacity of hydrogels as a function of their iodine content in the hydrogel; slope = 593 ± 30 HU per wt% of iodine; intercept = −122 ± 23 HU at tube voltage 50 kV; $R2$ = 0.995. n = 3 (B) coronal μCT-image of hydrogel pieces inside an Eppendorf, from left to right pieces, from formulation AUP160, AUP80, AUP40 and AUP0. (C) Sagittal μCT-image of hydrogel pieces inside an Eppendorf, from top to bottom pieces, from formulation AUP160, AUP80, AUP40 and AUP0. (D) Coronal μCT image of probe coated with formulation AUP160, in comparison with non-coated probe inside agarose brain phantom (0.6 wt%). (E) Post operational sagittal μCT image of flexible neural probe inside an *in vivo* mouse model. The probe was coated with material from formulation AUP160. The red Oval indicates the position of probe inside the hippocampus of the mouse.

radiodensity of the material. Hence, obtaining control over the radiodensity allows the user to tune the coating properties towards optimal visibility for their *in vivo* setting.[52,53]

3.6 CT-traceable coatings aid *in vivo* visualisation of neural implants

Given the promising results with the hydrogel samples, a verification experiment was needed to establish that similar results can be acquired when using a thin coating (≈50 μm) on a neural probe. Therefore, we continued our stepwise process and used hydrogel formulation AUP160 (49.4 mg mL^{-1} AATIPA, 587.1 HU) to coat our flexible probes. The higher AATIPA content for further experiments was chosen to ensure adequate radiodensity even when measuring 50 μm coatings. Fig. 5 illustrates that the smaller size of the coating does not interfere with our ability to visualize the coated probes.

The detection limits of the probe size were evaluated *in vitro* using probes of varying dimensions (40 × 40 μm^2, 70 × 70 μm^2, 100 × 120 μm^2, and 120 × 120 μm^2) and different coating thicknesses (1, 3 *versus* 5 layers). Our results indicate that coating thickness is not a decisive factor for probe visibility, as even minimally coated probes were detectable. In contrast,

probe size played a crucial role, with only the larger probes (100 × 120 μm^2 and 120 × 120 μm^2) being consistently visualized, while the smaller sizes were difficult to distinguish from the background, as shown in Fig. S19.

Finally, we repeated this experiment in an *in vivo* mouse model. Fig. 6 depicts the sagittal post-operative μCT-scans of the mouse brain. These experiments demonstrate that the coatings enable *in vivo* visualization of the implants. Additionally, the scans show that that no major mechanical failures have occurred during the implantation procedures. In SI Fig. S20 and S21, 3D visualisations of the probe inside the mouse model are depicted to support our findings.

3.7 Hydrogel does not lead to reduced neuronal density or increased inflammation

To assess potential neurotoxic and inflammatory effects of the AUP160 hydrogel coating, we quantified neuronal density (NeuN), astrocyte reactivity (GFAP) and microglial activation (Iba1) around the implantation tract in mouse brain tissue. The markers were measured at increasing distance from the implantation tract boundary (0–100 μm, 100–200 μm, 200–300 μm, and 300–400 μm) to evaluate the spatial extent of any tissue damage.

Analysis of NeuN immunostaining showed a significant effect of distance from lesion boundary ($p < 0.0001$ for all distance categories), with neural density increasing systematically with distance from the implantation tract. This pattern was expected, as implantation causes localized tissue damage that diminishes with distance.[48] No significant difference in neuronal density was found between Glass and AUP160 conditions ($p = 0.137$), indicating that the hydrogel coating does not cause additional neuronal loss compared to the glass control (Fig. 7A). Immediately adjacent to the implant (0–100 μm), neuronal density was 3196 ± 263 neurons per mm^2 for glass controls and 3279 ± 276 neurons per mm^2 for hydrogel-coated probes, followed by increase until "baseline values" at 300–400 μm (glass: 4877 ± 115 neurons per mm^2; AUP160: 4759 ± 155 neurons per mm^2), demonstrating that the AUP160 hydrogel coating is biocompatible and does not exacerbate implantation-induced neuronal damage as compared to glass controls.

Complementary analysis of astrocyte and microglial markers, similarly demonstrated that the hydrogel did not elicit an

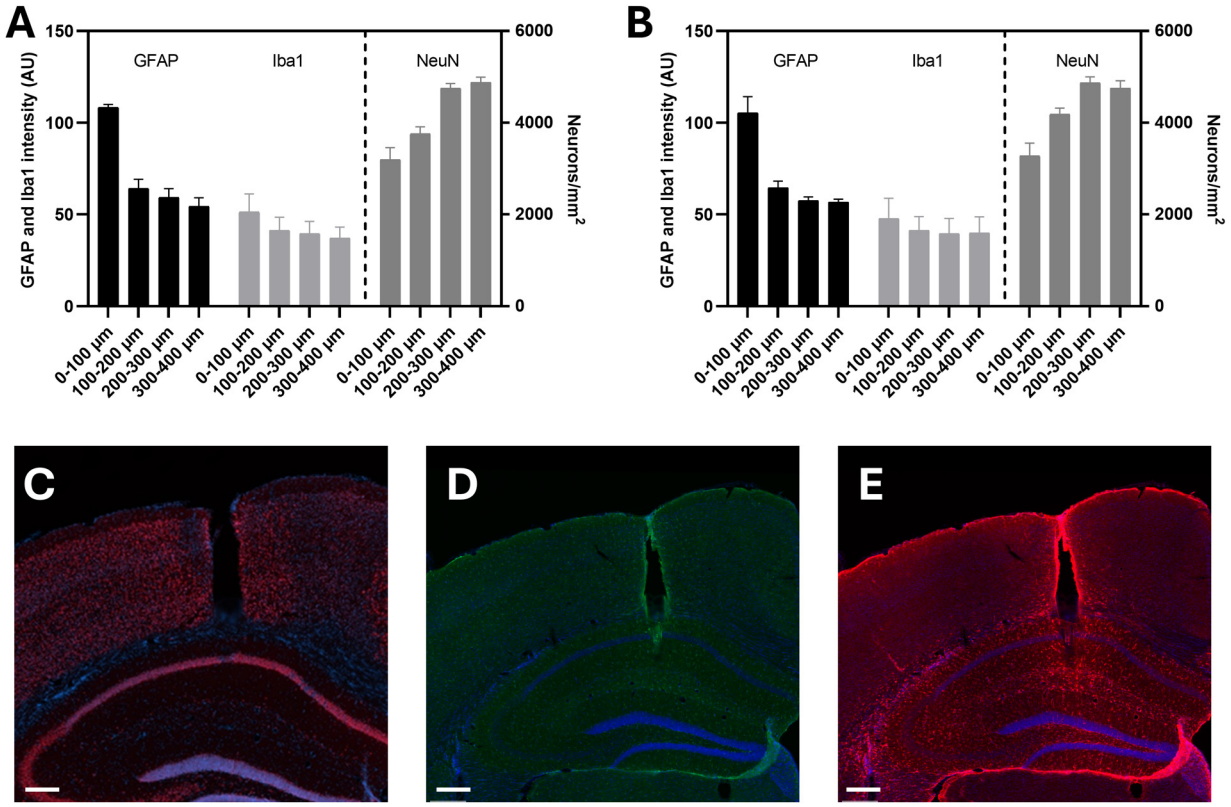

Fig. 7 Bar graphs showing mean GFAP and Iba1 fluorescent intensity (AU: arbitrary units) as a function of distance from implantation tract on the left *Y*-axis and neural density (neurons per mm^2) on the right *Y*-axis for (A) glass control probes and (B) AUP160 coated flexible probes. Bars represent mean ± SD with statistical comparisons performed using mixed-effects modelling accounting for nested data structure (multiple slices within animals). *N* = 3 animals and 3 slices per animal at 6 weeks post-implantation. (C) Representative sample of a single section stained with anti-NeuN after a AUP160 coated probe implantation. (red: anti-NeuN; blue: DAPI). (D) Representative sample of a single section stained with Iba1 after a AUP160 coated probe implantation. (green: Iab1; blue: DAPI). (E) Representative sample of a single section stained with GFAP after a AUP160 coated probe implantation. (red: GFAP; blue: DAPI). Scale bars equal 250 μm.

increased inflammatory response. Both GFAP (astrocytes) and Iba1 (microglia) intensities showed characteristic distance-dependent gradients ($p < 0.001$), with intensity values declining progressively with distance from the tract. The mixed-effects model analysis did not lead to significant differences between glass and hydrogel coated probes for either GFAP ($p = 0.885$) or Iba1 ($p = 0.993$). This suggests similar patterns of astrocytic and microglial responses across both conditions.

Specifically, at 0–100 μm distance, GFAP intensity was 108 ± 1.6 AU in the glass control condition and 105 ± 8.9 AU in the hydrogel-coated condition. Both conditions gradually declined until (51 ± 3.9 AU *vs.* 54 ± 0.9 AU), respectively at 400–500 μm. Iba1 intensity amounted 51 ± 9.9 AU in the glass condition and 48 ± 11.1 AU in the hydrogel-coated condition at 0–100 μm distance and the spatial gradient closely mirrored that observed for astrocytes. Here, the 400–500 μm zone showed 36 ± 6.3 AU *vs.* 39 ± 8.7 AU for the respective conditions.

The absence of significant differences between the glass control and the hydrogel coated condition over the different markers indicates that the AUP160 hydrogel coating does not exacerbate the inflammatory response compared to glass controls. The similar profiles between conditions indicate that the interoperative imaging and mechanical benefits provided by the hydrogel coating do not come at the cost of increased chronic inflammation at the timepoint evaluated (6 weeks).

4. Conclusions

In summary, this study demonstrated the successful development of radiopaque AUP hydrogel coatings, targeting neural applications. Incorporation of AATIPA provided tuneable radiodensity, reaching 587 ± 176 HU for formulation AUP160, without compromising gel fraction (>94%) or mechanical integrity (storage modulus 147–195 kPa, compressive modulus ≈0.5 MPa). Additionally, the hydrogel retained its biocompatibility even at the highest AATIPA loading, evidenced by a cell viability above the 70% ISO10993 threshold.

The hydrogel formulations were used as coating (≈60 μm) onto flexible probes, which doubled the implants' critical buckling force from 15.2 ± 2.0 mN (uncoated) to 33.0 ± 1.5 mN. Subsequently, these mechanical improvements led to successful insertion into 0.6% agarose brain phantoms. Finally, the flexible probes were implanted and in the presence of the AATIPA coating, μCT visualisation was achieved in a hippocampal mouse model. The histological analysis showed no significant differences between the hydrogel-coated and glass control probes, confirming the absence of hydrogel-induced neurotoxicity.

Overall, the dual-function coating strategy both enhanced the implantability and provided a more compliant interface post-implantation. Additionally, it allowed for *in vivo* imaging, offering a novel strategy for post-operative monitoring without the need for animal sacrifice.

Author contributions

CRediT: conceptualization: AP, FP, KK, SVV; data curation: AP; formal analysis: AP, LVD, JWS; funding acquisition: JM, RR, SVV; investigation: AP, FP, WVL, KK, LVD, JWS; methodology: AP, FP, WVL, KK, LVD; project administration: AP, SVV; resources: AS, JM, RR, SVV; software; supervision: AS, JM, RR, SVV; validation: AP; visualization: AP, WVL, LVD, JWS; writing – original draft: AP, FP, WVL, JWS; writing – review & editing: AP, RR, SVV, JM.

Conflicts of interest

The authors declare no conflict of interest.

Data availability

The data supporting this article have been included as part of the supplementary information (SI). Supplementary information is available. See DOI: https://doi.org/10.1039/d5tb01967b.

Acknowledgements

The research was funded by Ghent University Special Research Fund-BOF (grant number 01G02722). The authors gratefully acknowledge Sara Neyt of the Core ARTH infinity facility at Ghent University (Belgium) for the use and support with μCT imaging. The Health Innovation and Research Institute of UZ Ghent (Belgium) was involved in the histological analysis. The authors also thank the NMR Expertise Centre (Ghent University, Krijgslaan 281 S4, 9000 Ghent, Belgium) for the usage of their ^{1}H NMR equipment. A. G. S. and K. K. acknowledge the support of FWO (grant numbers 1002620N and 1247425N).

Notes and references

1 K. T. Thakur, E. Albanese, P. Giannakopoulos, N. Jette, M. Linde, M. J. Prince, T. J. Steiner and T. Dua, in *Mental, Neurological, and Substance Use Disorders: Disease Control Priorities*, ed. V. Patel, D. Chisholm, T. Dua, R. Laxminarayan and M. E. Medina-Mora, Washington (DC), 3rd edn, 2016, vol. 4, DOI: 10.1596/978-1-4648-0426-7_ch5.
2 V. Krishna and A. Fasano, *Neurotherapeutics*, 2024, **21**, e00371.
3 A. M. Lozano, N. Lipsman, H. Bergman, P. Brown, S. Chabardes, J. W. Chang, K. Matthews, C. C. McIntyre, T. E. Schlaepfer, M. Schulder, Y. Temel, J. Volkmann and J. K. Krauss, *Nat. Rev. Neurol.*, 2019, **15**, 148–160.
4 C. Armstrong, E. Krook-Magnuson, M. Oijala and I. Soltesz, *Nat. Protoc.*, 2013, **8**, 1475–1493.
5 J. T. Paz, T. J. Davidson, E. S. Frechette, B. Delord, I. Parada, K. Peng, K. Deisseroth and J. R. Huguenard, *Nat. Neurosci.*, 2013, **16**, 64–70.

6 H. Chen and Y. Fang, *MRS Bull.*, 2023, **48**, 484–494.
7 A. Lecomte, E. Descamps and C. Bergaud, *J. Neural Eng.*, 2018, **15**, 031001.
8 J. Subbaroyan, D. C. Martin and D. R. Kipke, *J. Neural Eng.*, 2005, **2**, 103–113.
9 N. Sharafkhani, A. Z. Kouzani, S. D. Adams, J. M. Long, G. Lissorgues, L. Rousseau and J. O. Orwa, *J. Neurosci. Methods*, 2022, **365**, 109388.
10 M. Gulino, D. Kim, S. Pane, S. D. Santos and A. P. Pego, *Front. Neurosci.*, 2019, **13**, 689.
11 X. Wan, M. Liu, F. Zhang, L. P. Xu and S. Wang, *Angew. Chem., Int. Ed.*, 2025, e202425552.
12 W. Shen, L. Karumbaiah, X. Liu, T. Saxena, S. Chen, R. Patkar, R. V. Bellamkonda and M. G. Allen, *Microsyst. Nanoeng.*, 2015, **1**, 15010.
13 M. R. Abidian and D. C. Martin, *Adv. Funct. Mater.*, 2009, **19**, 573–585.
14 K. C. Spencer, J. C. Sy, K. B. Ramadi, A. M. Graybiel, R. Langer and M. J. Cima, *Sci. Rep.*, 2017, **7**, 1952.
15 G. L. Mario Cheong, K. S. Lim, A. Jakubowicz, P. J. Martens, L. A. Poole-Warren and R. A. Green, *Acta Biomater.*, 2014, **10**, 1216–1226.
16 A. Golabchi, B. Wu, B. Cao, C. J. Bettinger and X. T. Cui, *Biomaterials*, 2019, **225**, 119519.
17 Q. Yang, B. Wu, J. R. Eles, A. L. Vazquez, T. D. Y. Kozai and X. T. Cui, *Adv. Biosyst.*, 2020, **4**, e1900287.
18 X. Chen, Y. Feng, P. Zhang, Z. Ni, Y. Xue and J. Liu, *Adv. Mater.*, 2025, **37**, e2413476.
19 Y. Xue, X. Chen, F. Wang, J. Lin and J. Liu, *Adv. Mater.*, 2023, **35**, 2304095.
20 J. Zhang, L. Wang, Y. Xue, I. M. Lei, X. Chen, P. Zhang, C. Cai, X. Liang, Y. Lu and J. Liu, *Adv. Mater.*, 2023, **35**, 2209324.
21 S. Colachis, P. D. Ganzer, D. A. Friedenberg and G. Sharma, in *Handbook of Neuroengineering*, ed. N. V. Thakor, Springer Nature Singapore, Singapore, 2020, pp. 1–33, DOI: 10.1007/978-981-15-2848-4_119-1.
22 S. Pimenta, J. A. Rodrigues, F. Machado, J. F. Ribeiro, M. J. Maciel, O. Bondarchuk, P. Monteiro, J. Gaspar, J. H. Correia and L. Jacinto, *Front. Neurosci.*, 2021, **15**, 663174.
23 C. Cointe, A. Laborde, L. G. Nowak, D. N. Arvanitis, D. Bourrier, C. Bergaud and A. Maziz, *Microsyst. Nanoeng.*, 2022, **8**, 21.
24 D. Kleinfeld, L. Luan, P. P. Mitra, J. T. Robinson, R. Sarpeshkar, K. Shepard, C. Xie and T. D. Harris, *Neuron*, 2019, **103**, 1005–1015.
25 L. Luan, R. Yin, H. Zhu and C. Xie, *Annu. Rev. Biomed. Eng.*, 2023, **25**, 185–205.
26 S. Felix, K. Shah, D. George, V. Tolosa, A. Tooker, H. Sheth, T. Delima and S. Pannu, *Annu. Int. Conf. IEEE Eng. Med. Biol. Soc.*, 2012, **2012**, 871–874.
27 G. Lind, C. E. Linsmeier, J. Thelin and J. Schouenborg, *J. Neural Eng.*, 2010, **7**, 046005.
28 S. Takeuchi, D. Ziegler, Y. Yoshida, K. Mabuchi and T. Suzuki, *Lab Chip*, 2005, **5**, 519–523.
29 Z. Xiang, S.-C. Yen, N. Xue, T. Sun, W. M. Tsang, S. Zhang, L.-D. Liao, N. V. Thakor and C. Lee, *J. Micromech. Microeng.*, 2014, **24**, 065015.
30 L. U. Sneddon, L. G. Halsey and N. R. Bury, *J. Exp. Biol.*, 2017, **220**, 3007–3016.
31 J. R. Rangarajan, G. Vande Velde, F. van Gent, P. De Vloo, T. Dresselaers, M. Depypere, K. van Kuyck, B. Nuttin, U. Himmelreich and F. Maes, *Sci. Rep.*, 2016, **6**, 38058.
32 B. Kiraly, D. Balazsfi, I. Horvath, N. Solari, K. Sviatko, K. Lengyel, E. Birtalan, M. Babos, G. Bagamery, D. Mathe, K. Szigeti and B. Hangya, *Nat. Commun.*, 2020, **11**, 4686.
33 K. Kolouchova, Q. Thijssen, O. Groborz, L. Van Damme, J. Humajova, P. Matous, A. Quaak, M. Dusa, J. Kucka, L. Sefc, M. Hruby and S. Van Vlierberghe, *Adv. Healthcare Mater.*, 2025, **14**, 2402256.
34 O. Groborz, K. Kolouchova, L. Parmentier, A. Szabó, B. Van Durme, D. Dunlop, T. Slanina and S. Van Vlierberghe, *ACS Appl. Eng. Mater.*, 2024, **2**, 811–817.
35 M. Minsart, N. Deroose, L. Parmentier, S. Van Vlierberghe, A. Mignon and P. Dubruel, *Macromol. Biosci.*, 2023, **23**, e2200341.
36 M. Markovic, J. Van Hoorick, K. Holzl, M. Tromayer, P. Gruber, S. Nurnberger, P. Dubruel, S. Van Vlierberghe, R. Liska and A. Ovsianikov, *J. Nanotechnol. Eng. Med.*, 2015, **6**, 0210011–0210017.
37 F. M. Muller, C. Vanhove, B. Vandeghinste and S. Vandenberghe, *Med. Phys.*, 2022, **49**, 3121–3133.
38 T. K. Meyvis, B. G. Stubbe, M. J. Van Steenbergen, W. E. Hennink, S. C. De Smedt and J. Demeester, *Int. J. Pharm.*, 2002, **244**, 163–168.
39 N. Pien, N. Deroose, M. Meeremans, C. Perneel, C. S. Popovici, P. Dubruel, C. De Schauwer and S. Van Vlierberghe, *Biomater. Adv.*, 2024, **162**, 213923.
40 S. Nemir, H. N. Hayenga and J. L. West, *Biotechnol. Bioeng.*, 2010, **105**, 636–644.
41 G. J. Rodriguez-Rivera, M. Green, V. Shah, K. Leyendecker and E. Cosgriff-Hernandez, *J. Biomed. Mater. Res., Part A*, 2024, **112**, 1200–1212.
42 M. B. Browning, S. N. Cereceres, P. T. Luong and E. M. Cosgriff-Hernandez, *J. Biomed. Mater. Res., Part A*, 2014, **102**, 4244–4251.
43 S. Cereceres, Z. Lan, L. Bryan, M. Whitely, T. Wilems, N. Fabela, C. Whitfield-Cargile and E. Cosgriff-Hernandez, *Ann. Biomed. Eng.*, 2020, **48**, 953–967.
44 C. Schizas and D. Karalekas, *J. Mech. Behav. Biomed. Mater.*, 2011, **4**, 99–106.
45 M. H. Khalili, C. J. Williams, C. Micallef, F. Duarte-Martinez, A. Afsar, R. Zhang, S. Wilson, E. Dossi, S. A. Impey, S. Goel and A. I. Aria, *ACS Appl. Polym. Mater.*, 2023, **5**, 1180–1190.
46 J. Song, C. Michas, C. S. Chen, A. E. White and M. W. Grinstaff, *Adv. Healthcare Mater.*, 2020, **9**, e1901217.
47 Z. Drira and V. K. Yadavalli, *J. Mech. Behav. Biomed. Mater.*, 2013, **18**, 20–28.

48 H. C. Lee, F. Ejserholm, J. Gaire, S. Currlin, J. Schouenborg, L. Wallman, M. Bengtsson, K. Park and K. J. Otto, *J. Neural Eng.*, 2017, **14**, 036026.
49 Z. J. Chen, G. T. Gillies, W. C. Broaddus, S. S. Prabhu, H. Fillmore, R. M. Mitchell, F. D. Corwin and P. P. Fatouros, *J. Neurosurg.*, 2004, **101**, 314–322.
50 K. J. Seo, P. Artoni, Y. Qiang, Y. Zhong, X. Han, Z. Shi, W. Yao, M. Fagiolini and H. Fang, *Adv. Biosyst.*, 2019, **3**, e1800276.
51 K. Kolouchova, N. Pien, N. F. Cetin, Z. Cernochova, J. Van Meerssche, M. Slouf, A.-A.-A. Bara, O. Groborz, M. Hruby and S. Van Vlierberghe, *Nanoscale*, 2025, **17**(32), 18709–18726.
52 C. K. Emonde, M. E. Eggers, M. Wichmann, C. Hurschler, M. Ettinger and B. Denkena, *ACS Biomater. Sci. Eng.*, 2024, **10**, 1323–1334.
53 K. Kolouchova, J. Humajova, P. Matous, N. Ritter, L. Van Damme, M. Hovorakova, Z. Pavlikova, L. Dalecka, K. Steklikova, J. Zeman, J. Kucka, M. Hruby, O. Groborz, L. Sefc and S. Van Vlierberghe, *Commun. Mater.*, 2025, **6**, 112.

